Article

Mechanism Analysis of Roadway Rockbursts Induced by Dynamic Mining Loading and Its Application

Zheng-yi Wang [1] **, Lin-ming Dou** [1,*] **and Gui-feng Wang** [1]

Key Laboratory of Deep Coal Resource Mining, Ministry of Education of China, School of Mines,
China University of Mining and Technology, Xuzhou 221116, China; 15062193699@163.com (Z.-y.W.);
wgfskl@163.com (G.-f.W.)

*   Correspondence: lmdou@cumt.edu.cn; Tel.: +86-139-5226-1972

check for
updates

Abstract: Roadway rockbursts seriously restrict the safety production of coal mines; however, the interaction between dynamic loads and roadway surrounding rocks has not been fully considered in existing studies. A dynamic failure analysis model of anchoring supporting structures was established to analyze dynamic effects of stress waves. Taking a rockburst in LW402103 of the Hujiahe coal mine as the case, the theoretical model was well applied and verified. The static cumulative resistance Q_s (210.5 kN) which was incurred by deformation of rocks provided the basis (81.93% in the overall real-time resistance Q) of dynamic failures. However, the additional impact resistance Q_d (46.43 kN) brought about by the energy release in the failure process of elastic zones triggered impact failures. As a result, under conditions that the overall real-time resistance Q (256.93 kN) exceeded the ultimate resistance $[Q]$ (250.8 kN), the dynamic failure of supports occurred. The in situ application was implemented by taking pressure-relief measures and parameter optimizations of roadway supports, which achieved an effective prevention of rockbursts.

Keywords: rockburst; dynamic failure; anchoring supporting structure; pressure-relief measure

1. Introduction

A rockburst is a representative dynamic disaster encountered during coal mining and it impacts the safety and production of coal mines [1]. Ever since the first recorded rockburst occurred in England in 1738, rockburst events have been reported in all coal-mining countries. Numerous researchers across the world have investigated rockbursts [2–7] and concluded that most rockbursts (approximate 85%) take place in roadways because of being disturbed by an external hypocentre, and dynamic damages to surrounding rocks of roadways appear under conditions superposing static and dynamic loads [8,9].

In previous research on the mechanisms of dynamic failure of roadways [10,11], the wave function expansion method was used to obtain the distributions of stress, acceleration, displacement, and dynamic stress concentration index in roadway surrounding rocks and linings under dynamic loading; however, in essence, the bearing structure of rock-bolt systems in a coal roadway differs from its lining structure. Therefore, the roadway anchoring indicates that the anchors are in the strain softening state, so the bolt resistance and the surrounding rock strength inevitably changes under the action of microseisms. In addition, the bearing structure of rock-bolt systems cannot be substituted by the lining structure for the parameters of the latter if they are unchanged. Moreover, by using the wave function expansion method, generally scholars only take into account the stress states of the lining structures and the surrounding rocks under peak loading, while the dynamic action process is ignored. Additionally, owing to this calculation method being too complex, one can only attain approximate solutions. The strong-soft-strong (3S) structural model for preventing the occurrence of rockbursts was constructed [12], which has the following characteristics. For example, the strength

characteristics of the structure itself and the capabilities including wave absorption, stress adjustment and energy absorption. They also deduced the energy rule and strength criterion of the small-sized inner support structures which were destroyed by rockburst. While this model provides guidance for the prevention and control over dynamic disasters in actual roadways, it does not consider the time-dependent effects of rockbursts, let alone the dynamic failure of elastic zones in surrounding rocks of roadway. In addition, this model is also not capable of clarifying the impact force sources of a roadway rockburst.

According to the existing governing theory for the behaviors of rock masses in a complicated hierarchy of discontinuous block structures, which have self-balancing characteristics with regard to the stress field [13], a theoretical model of discontinuous overlying rocks under cross-feed action of the blocky rock-support system was built [14]. The influences of performance of the support upon the dynamics response of the overlying block rocks were investigated under conditions that the shock loads propagated in the rocks was as pendulum-type waves. The propagation law of stress waves can be acquired by considering surrounding rocks and roadway supporting as rigid and damping blocks. However, the dynamic failure characteristics of anchoring structures still need to be studied. Moreover, it is demonstrated in existing research that the energies released during the damage of primary load-bearing structures serves as the major energy source of dynamic disasters [15]. A rockburst occurs in a roadway only if the bearing structures of the rock-bolt system are unable to resist the dynamic loads resulting from instantaneous failure of elastic zones in surrounding rocks. Furthermore, the action of microseisms and the dynamic failure of a roadway both present time-dependent characteristics, thereby creating a dynamic failure analysis of rockbursts in roadways failing to accord with real conditions.

Therefore, based on the propagation of stress waves, and the characteristics of bearing structures in roadway surrounding rocks, an analysis model for dynamic failures of anchoring roadway supporting structures was established under mining-induced dynamic loading. Furthermore, the impact failure criteria of the bolt support system were deduced, with corresponding preventative measures suggested.

2. Analysis of Dynamic Failure of Supporting Structures for an Anchored Roadway

2.1. Modelling

The analysis object is focused on a representative roadway with straight walls, which can be simplified as the semicircular roadway. Then, the dynamic analysis model under mining-induced dynamic loading was built, as shown in Figure 1. For the sake of convenience, the arch roadway with straight walls can be simplified as the semicircular roadway. Meanwhile, the primary stresses in the surrounding rocks were considered to be in the state of hydrostatic pressure, and thus regarded as a plane strain problem. It can be seen from Figure 1 that zones A, B and C refer to the bearing structure of the rock-bolt system, the plastic zone (stress-concentrated area) outside zone A and the elastic zone, respectively. All of these zones all belong to bearing zones. In addition, a, d, R_0, b, and R_p separately denote the length of bolts, row and line space of bolts, the radius of the roadway, the thickness of bearing structures of rock-bolt system and the plastic zone radius [16].

In Figure 1, L and E_{d0} represent the distance from the source of dynamic loads to the roadway center and the corresponding microseismic energy, respectively. Because the buried depth H meets the condition of $H >> R_0$ and an even higher order of magnitude lies between L and R_0, it can be assumed that stress waves take the same time to reach the bearing zones in surrounding rocks of roadways. Hence, the stress waves which propagate to surrounding rocks can be regarded as uniform distributions on the surface of bearing zones and shock waves induced by microseisms are considered to exert effects on surrounding rocks via normal incidence [12]. Since actual occurrence mechanisms of microseisms are so complex, the vibration wave can be appropriately simplified as a sine wave [17] and parameters (such as periods T and peak particle vibration velocity v_m) of vibration waves with the same energy can be assumed to be consistent enough to facilitate the theoretical analysis.
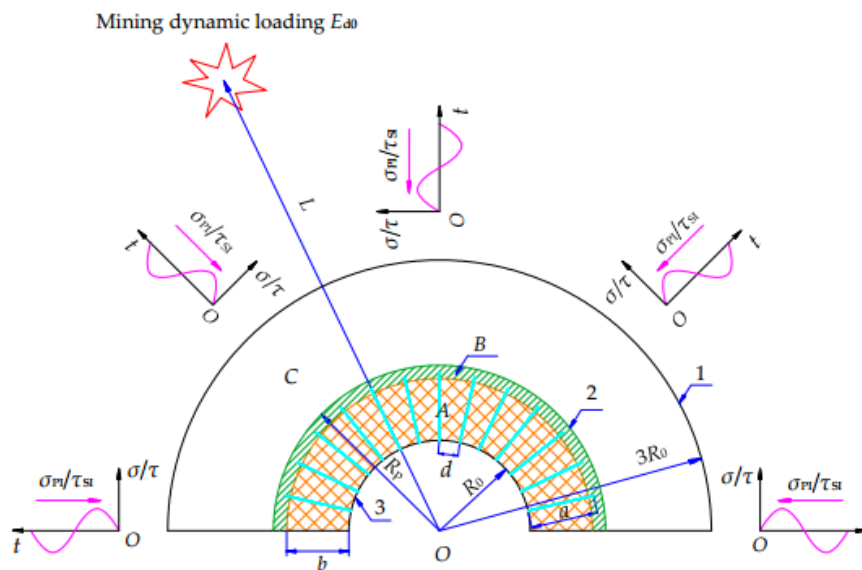
Figure 1. Mechanical model for the supporting structure of roadways under mining-induced dynamic loads.

The research zones ($R_0 \leq r \leq 3R_0$) which cover zones A and B along with some areas in zone C were discussed. Because the P-wave propagates faster than the S-wave, the time difference Δt of S and P-waves reaching the boundary 1 ($r = 3R_0$) is given by:

$$\Delta t = \frac{L - 3R_0}{c_S} - \frac{L - 3R_0}{c_P} \tag{1}$$

where c_P and c_S represent the propagation speeds (m·s^{-1}) of P and S waves in coal-rock media, respectively. If the head of incident P-wave arrives at the boundary 1 ($r = 3R_0$) at the moment of $t = 0$, the wave functions of dynamic stresses induced by incident P and S waves on the boundary 1 are given by:

$$\begin{cases} \sigma_{PI}(r,t) = \sigma_{Pm} \sin\left(\omega\left(t - \frac{3R_0 - r}{c_P}\right)\right) & ,t \geq 0 \\ \tau_{SI}(r,t) = \tau_{Sm} \sin\left(\omega\left((t - \Delta t) - \frac{3R_0 - r}{c_S}\right)\right) & ,t \geq \Delta t \end{cases} \tag{2}$$

where σ_{Pm} and τ_{Sm} represent the maximum value (MPa) of normal stress attributable to P-waves and the shear stress generated due to S-waves, separately.

As the P-wave (or S-wave) arrives at boundary 2 ($r = R_p$), the transmitted and reflected waves are derived correspondingly on boundary 2 between the elastic and plastic zones. Owing to that zones A and B belong to the limit equilibrium zone (in the post peak state), the relevant attenuation coefficient is large enough, which causes that the transmitted waves can be adequately dissipated after entering the limit equilibrium zone. Therefore, the influence of stress waves returned to the elastic zone (zone C) again, originated from transmitted waves, can be ignored. Under these circumstances, only the superposition effect of incident, and reflected, waves is worth analyzed. In accordance with reflection theorem for normal incidence of stress waves [17], the wave functions of dynamic stress produced due to reflected waves (P and S waves) on the boundary 2 are given by:

$$\begin{cases} \sigma_{PR} = -F\sigma_{Pm} \sin\left(\omega\left(t - \frac{3R_0 - 2R_p + r}{c_P}\right)\right) & ,t \geq \frac{3R_0 - R_p}{c_P} \\ \tau_{SR} = -F\tau_{Sm} \sin\left(\omega\left((t - \Delta t) - \frac{3R_0 - 2R_p + r}{c_S}\right)\right) & ,t \geq \Delta t + \frac{3R_0 - R_p}{c_S} \end{cases} \tag{3}$$

where $F = (1 - n)/(1 + n)$ and $n = (\rho_1 c_1)/(\rho_2 c_2)$. The n values 1.4 approximately for coal masses.

Peak values of the dynamic stresses σ_{Pm} and τ_{Sm} can be obtained [17], as to incident and reflected waves, $l = L - r$ and $l = L + r - 2R$, respectively. Based on existing monitoring data [18], a good fitting effect ($R^2 = 0.9395$) for the relationship between the peak vibration velocity v_m and microseismic energy E_{d0} is shown in Figure 2 and the corresponding expression is given by:

$$v_m = 0.0645 E_{d0}{}^{0.3566} \tag{4}$$

Based on Equation (4), v_m (m·s^{-1}) can be calculated (approximately) according to the value of E_{d0} (J).
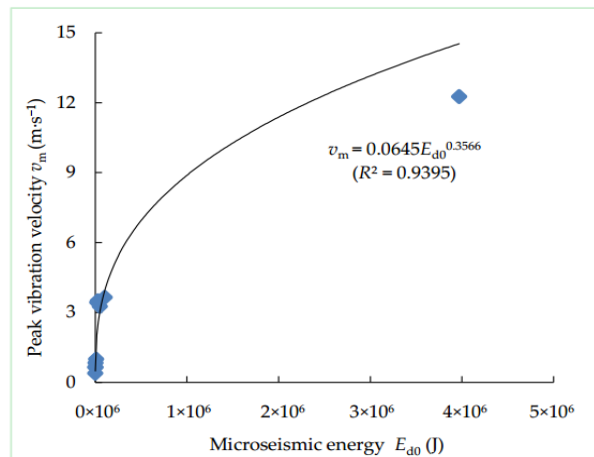

Figure 2. Fitting relationship between peak vibration velocity v_m and microseismic energy E_{d0}, presenting a power function relation.

2.2. Effects of Mining Dynamic Loading

The whole action process of dynamic loading starts from stress waves entering, to completely leaving, the area of interest, that is, from the moment when the head of incident P wave arrives at boundary 1 (when $t = 0$) to that when the tail of the reflected S-wave leaves boundary 1 (when $t = \Delta t + T + (6R_0 - 2R_p)/c_S$). The S-wave delays for Δt to reach the research area compared with the P-wave, the action process and superposition laws of the S-wave in the research area are consistent with those of the P-wave, therefore, only the P-wave is analyzed, which can provide references for the S-wave thereafter. Based on the transmission and superposition of stress waves, the action process was split into six time periods and Figure 3 shows the relevant position of the studied region and the stress waves in every time period.


(a)

Figure 3. *Cont.*

(b)

(c)

(d)

(e)
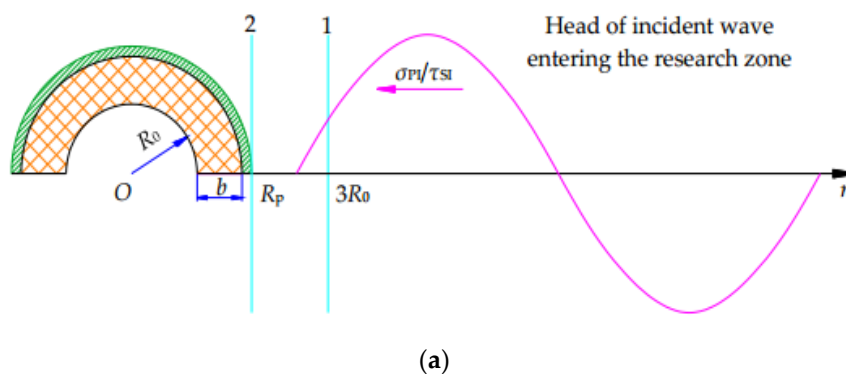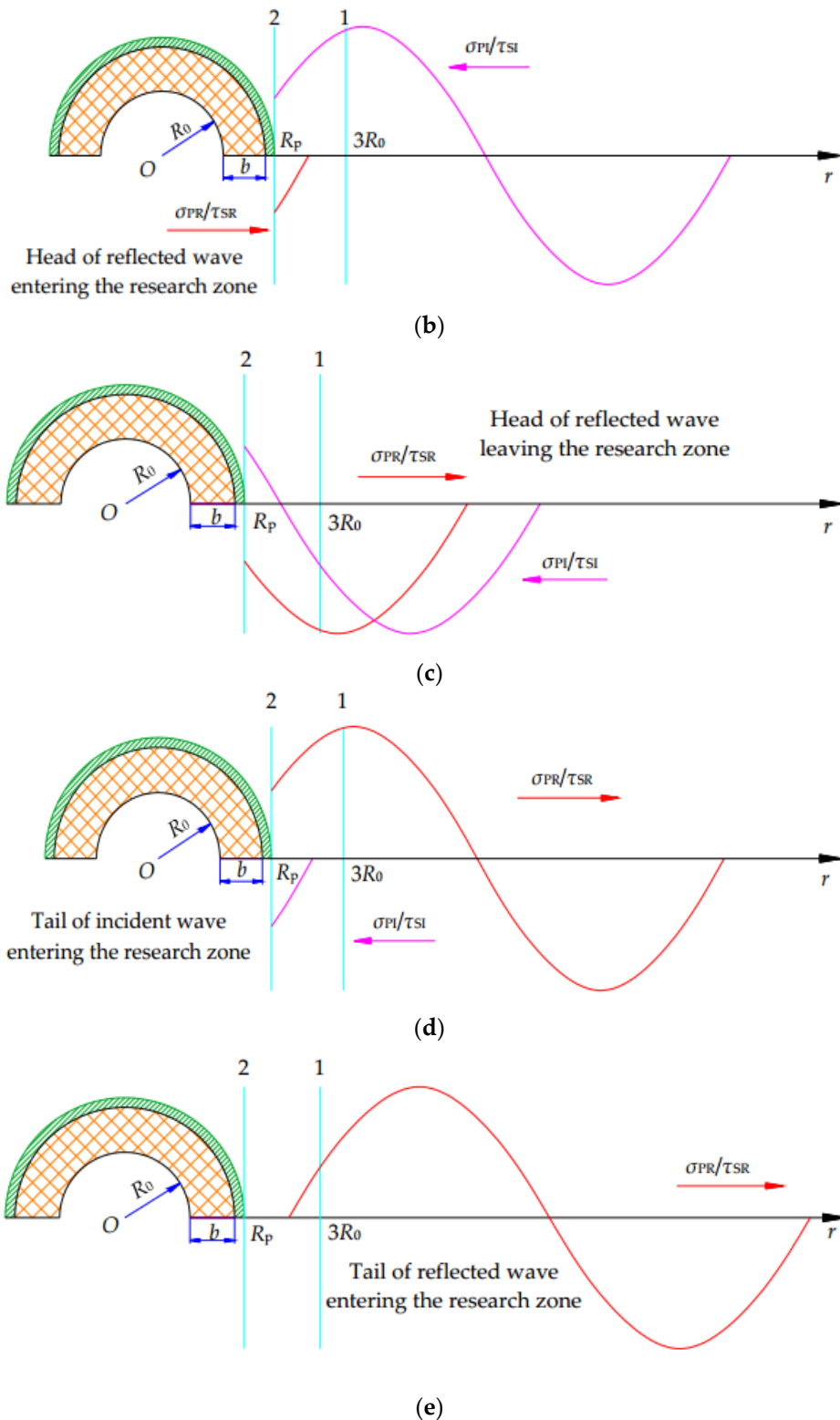
Figure 3. Five time periods divided based on action processes of stress waves, including: (**a**) first time period: head of incident wave entering the research zone; (**b**) second time period: head of reflected wave entering the research zone; (**c**) third time period: head of reflected wave leaving the research zone; (**d**) fourth time period: tail of incident wave entering the research zone; (**e**) fifth time period: tail of reflected wave entering the research zone.

The first time period ($0 < t \leq (3R_0 - R_p)/c_P$), as shown in Figure 3a, starts from the moment when the head of the incident wave arrives at boundary 1, to the head of the incident wave arriving at boundary 2. Spreading inwards, the incident wave has a time-variant range of influences. The unit bodies between boundaries 1 and 2 are impacted by the incident wave successively, so some parts of the research region are influenced by the incident P-wave. Besides, the influenced areas vary with time t. For example, the distance l_{P1} that the incident wave propagates in the analysis region meets the condition of $l_{P1} = c_P \cdot (t - 0) = c_P \cdot t$, and then the affected zone is in the range from $3R_0 - l_{P1}$ (namely $3R_0 - c_P \cdot t$) to $3R_0$, at a certain moment t ($0 < t \leq (3R_0 - R_p)/c_P$). Therefore, the dynamic stress attributable to the incident P-wave meets the condition of $\sigma_{PI} = \sigma_{PI}$ (r,t) (Equation (2)) to the region (($3R_0 - c_P \cdot t) \leq r \leq 3R_0$), while $\sigma_{PI} = 0$ for the remainder of the analysis region ($R_p \leq r < (3R_0 - c_P \cdot t)$). Furthermore, no analysis region was impacted by reflected waves in the first time period, so the corresponding stress imposed by reflected waves satisfies $\sigma_{PR} = 0$.

The second time period (($3R_0 - R_p)/c_P < t \leq (6R_0 - 2R_p)/c_P$) covers the duration from the moment when the head of the reflected wave reaches the boundary 2 to that when it arrives at boundary 1 (Figure 3b). The overall studied region was affected by the incident wave in this whole time period, so $\sigma_{PI} = \sigma_{PI}$ (r,t) (Equation (2)). However, the coal-rock units were impacted by the reflected wave propagating from boundary 2 to 1 successively. As a result, only parts of the research region were influenced by the reflected wave and the influenced areas varied with time t. The travelling distance l_{P2} of the reflected wave in the studied zone meets the condition of $l_{P2} = c_P \cdot (t - (3R_0 - R_p)/c_P)$ $= c_P \cdot t - 3R_0 + R_p$. Therefore, the range of the influenced zone extends from R_p to ($R_p + l_{P2}$) (i.e., $c_P \cdot t - 3R_0 + 2R_p$), at a moment t (($3R_0 - R_p)/c_P < t \leq (6R_0 - 2R_p)/c_P$). Therefore, the corresponding dynamic stress attributed to the reflected waves meets $\sigma_{PR} = \sigma_{PR}$ (r,t) (Equation (3)) for the region ($R_p \leq r < (c_P \cdot t - 3R_0 + 2R_p)$), while for the remainder of the studied region (($c_P \cdot t - 3R_0 + 2R_p) \leq r \leq 3R_0$), there is $\sigma_{PR} = 0$.

The third time period (($6R_0 - 2R_p)/c_P < t \leq T$), as shown in Figure 3c, begins from the moment when the head of the reflected wave reaches the boundary 1 to the moment as the tail of the incident wave arrives at boundary 1. Since the whole analysis region ($R_p \leq r \leq 3R_0$) was influenced by the incident and reflected waves in this whole time period, the dynamic stresses acted by the P-waves meet $\sigma_{PI} = \sigma_{PI}$ (r,t) (Equation (2)) and $\sigma_{PR} = \sigma_{PR}$ (r,t) (Equation (3)), separately.

As to the fourth time period ($T < t \leq (T + (3R_0 - R_p)/c_P)$), it starts from the moment when the tail of the incident wave reaches boundary 1, to the moment it arrives at boundary 2 (Figure 3d). It can be seen that the complete research zone was under the action of the reflected wave all the time in this time period, and therefore $\sigma_{PR} = \sigma_{PR}$ (r,t) (Equation (3)). However, coal-rock bodies were not influenced by the incident wave which successively propagated from the boundary 1 to 2. Thus, merely parts of the studied region were under the actions of the incident wave. Similarly, the influenced zone varied with time t as well. The distance l_{P4} of the incident wave travelling in the studied region meets $l_{P4} = c_P \cdot (t - T)$, and the scale of the influenced region expands from R_p to ($3R_0 - l_{P4}$) (namely $3R_0 - c_P \cdot (t - T)$), at a moment t ($T < t \leq (T + (3R_0 - R_p)/c_P)$). Therefore, the dynamic stress induced from the incident wave meets $\sigma_{PI} = \sigma_{PI}$ (r,t) (Equation (2)) for the region ($R_p \leq r < (3R_0 - c_P \cdot (t - T))$), while it meets $\sigma_{PI} = 0$ for the remaining research zone (($3R_0 - c_P \cdot (t - T)) \leq r \leq 3R_0$).

The fifth time period (($T + (3R_0 - R_p)/c_P) < t \leq (T + (6R_0 - 2R_p)/c_P)$) begins from the moment when the tail of the incident wave reaches the boundary 2, to when it arrives at boundary 1 (Figure 3e). The coal-rock bodies were not influenced by the incident wave in this time period, because the incident wave had left the studied region. Therefore, the corresponding dynamic stress applied by the incident wave was $\sigma_{PI} = 0$. However, the unit bodies got rid of the influence of the reflected wave propagating from the boundary 2 to 1 successively. As a result, it can be seen that only parts of the analysis region were impacted by the reflected wave and the influenced zone showed variation at different time moments t. $l_{P5} = c_P \cdot (t - (T + (3R_0 - R_p)/c_P)) = c_P \cdot (t - T) - 3R_0 + R_p$ is satisfied by the propagation distance l_{P5} of the reflected wave in the research region at a moment t (($T + (3R_0 - R_p)/c_P) < t \leq (T + (6R_0 - 2R_p)/c_P)$), so the scope of the zone under the action of the wave at this time t enlarges from

$(R_\mathrm{P} + l_{\mathrm{P}5})$ (i.e., $c_\mathrm{P} \cdot (t - T) - 3R_0 + 2R_\mathrm{P}$) to $3R_0$. Therefore, the dynamic stress induced from reflected waves meets $\sigma_{\mathrm{PR}} = \sigma_{\mathrm{PR}}(r,t)$ (Equation (3)) for the region $((c_\mathrm{P} \cdot (t - T) - 3R_0 + 2R_\mathrm{P}) \le r \le 3R_0)$, while it satisfies $\sigma_{\mathrm{PR}} = 0$ for the remaining research zone, which satisfies $R_\mathrm{P} \le r < (c_\mathrm{P} \cdot (t - T) - 3R_0 + 2R_\mathrm{P})$.

The sixth time period $((T + (6R_0 - 2R_\mathrm{P})/c_\mathrm{P}) < t \le (\Delta t + T + (6R_0 - 2R_\mathrm{P})/c_\mathrm{S}))$ starts from the moment when the tail of the reflected P-wave leaves boundary 1, to the moment that the tail of the reflected S-wave departs from boundary 1, during which time the analysis region is not under P-wave loading anymore. Because the dynamic stresses induced by P-waves (the incident and reflected) meet $\sigma_{\mathrm{PI}} = 0$ and $\sigma_{\mathrm{PR}} = 0$ in this time period, the corresponding action processes is not shown in Figure 3.

Table 1 lists the wave functions for P-waves (the incident and reflected) in every time period. Moreover, the research area is not yet affected by the S-wave when $0 < t \le \Delta t$. From the moment when the head of the incident S-wave reaches boundary 1 (when $t = \Delta t$) to that when the tail of the reflected S-wave departs from boundary 1 (when $t = \Delta t + T + (6R_0 - 2R_\mathrm{P})/c_\mathrm{S}$), the action of the S-wave can be obtained by referring to that of the P-wave (Table 2).

Table 1. P-wave functions according to the division of time periods in Figure 3.

No.	Time Period	Incident P-Wave	Reflected P-Wave
1	$0 < t \le \dfrac{3R_0 - R_\mathrm{P}}{c_\mathrm{P}}$	$\sigma_{\mathrm{PI}} = \begin{cases} 0 & , R_\mathrm{P} \le r < (3R_0 - c_\mathrm{P}t) \\ \sigma_{\mathrm{PI}}(r,t) & , (3R_0 - c_\mathrm{P}t) \le r \le 3R_0 \end{cases}$	$\sigma_{\mathrm{PR}} = 0$
2	$\dfrac{3R_0 - R_\mathrm{P}}{c_\mathrm{P}} < t \le \dfrac{6R_0 - 2R_\mathrm{P}}{c_\mathrm{P}}$	$\sigma_{\mathrm{PI}} = \sigma_{\mathrm{PI}}(r,t)$	$\sigma_{\mathrm{PR}} = \begin{cases} \sigma_{\mathrm{PR}}(r,t) & , R_\mathrm{P} \le r < (c_\mathrm{P}t - 3R_0 + 2R_\mathrm{P}) \\ 0 & , (c_\mathrm{P}t - 3R_0 + 2R_\mathrm{P}) \le r \le 3R_0 \end{cases}$
3	$\dfrac{6R_0 - 2R_\mathrm{P}}{c_\mathrm{P}} < t \le T$	$\sigma_{\mathrm{PI}} = \sigma_{\mathrm{PI}}(r,t)$	$\sigma_{\mathrm{PR}} = \sigma_{\mathrm{PR}}(r,t)$
4	$T < t \le \left(T + \dfrac{3R_0 - R_\mathrm{P}}{c_\mathrm{P}}\right)$	$\sigma_{\mathrm{PI}} = \begin{cases} \sigma_{\mathrm{PI}}(r,t) & , R_\mathrm{P} \le r < (3R_0 - c_\mathrm{P}(t - T)) \\ 0 & , (3R_0 - c_\mathrm{P}(t - T)) \le r \le 3R_0 \end{cases}$	$\sigma_{\mathrm{PR}} = \sigma_{\mathrm{PR}}(r,t)$
5	$\left(T + \dfrac{3R_0 - R_\mathrm{P}}{c_\mathrm{P}}\right) < t \le \left(T + \dfrac{6R_0 - 2R_\mathrm{P}}{c_\mathrm{P}}\right)$	$\sigma_{\mathrm{PI}} = 0$	$\sigma_{\mathrm{PR}} = \begin{cases} 0 & , R_\mathrm{P} \le r < (c_\mathrm{P}(t - T) - 3R_0 + 2R_\mathrm{P}) \\ \sigma_{\mathrm{PR}}(r,t) & , (c_\mathrm{P}(t - T) - 3R_0 + 2R_\mathrm{P}) \le r \le 3R_0 \end{cases}$
6	$\left(T + \dfrac{6R_0 - 2R_\mathrm{P}}{c_\mathrm{P}}\right) < t \le \left(\Delta t + T + \dfrac{6R_0 - 2R_\mathrm{P}}{c_\mathrm{S}}\right)$	$\sigma_{\mathrm{PI}} = 0$	$\sigma_{\mathrm{PR}} = 0$

Table 2. S-wave functions according to the division of time periods in Figure 3.

No.	Time Period	Incident S-Wave	Reflected S-Wave
1	$0 < t \le \Delta t$	$\tau_{\mathrm{SI}} = 0$	$\tau_{\mathrm{SR}} = 0$
2	$\Delta t < t \le \left(\Delta t + \dfrac{3R_0 - R_\mathrm{P}}{c_\mathrm{S}}\right)$	$\tau_{\mathrm{SI}} = \begin{cases} 0 & , R_\mathrm{P} \le r < (3R_0 - c_\mathrm{S}(t - \Delta t)) \\ \tau_{\mathrm{SI}}(r,t) & , (3R_0 - c_\mathrm{S}(t - \Delta t)) \le r \le 3R_0 \end{cases}$	$\tau_{\mathrm{SR}} = 0$
3	$\left(\Delta t + \dfrac{3R_0 - R_\mathrm{P}}{c_\mathrm{S}}\right) < t \le \left(\Delta t + \dfrac{6R_0 - 2R_\mathrm{P}}{c_\mathrm{S}}\right)$	$\tau_{\mathrm{SI}} = \tau_{\mathrm{SI}}(r,t)$	$\tau_{\mathrm{SR}} = \begin{cases} \tau_{\mathrm{SR}}(r,t) & , R_\mathrm{P} \le r \le (c_\mathrm{S}(t - \Delta t) - 3R_0 + 2R_\mathrm{P}) \\ 0 & , (c_\mathrm{S}(t - \Delta t) - 3R_0 + 2R_\mathrm{P}) < r \le 3R_0 \end{cases}$
4	$\left(\Delta t + \dfrac{6R_0 - 2R_\mathrm{P}}{c_\mathrm{S}}\right) < t \le (\Delta t + T)$	$\tau_{\mathrm{SI}} = \tau_{\mathrm{SI}}(r,t)$	$\tau_{\mathrm{SR}} = \tau_{\mathrm{SR}}(r,t)$
5	$(\Delta t + T) < t \le \left(\Delta t + T + \dfrac{3R_0 - R_\mathrm{P}}{c_\mathrm{S}}\right)$	$\tau_{\mathrm{SI}} = \begin{cases} \tau_{\mathrm{SI}}(r,t) & , R_\mathrm{P} \le r \le (3R_0 - c_\mathrm{P}(t - \Delta t - T)) \\ 0 & , (3R_0 - c_\mathrm{P}(t - \Delta t - T)) \le r < 3R_0 \end{cases}$	$\tau_{\mathrm{SR}} = \tau_{\mathrm{SR}}(r,t)$
6	$\left(\Delta t + T + \dfrac{3R_0 - R_\mathrm{P}}{c_\mathrm{S}}\right) < t \le \left(\Delta t + T + \dfrac{6R_0 - 2R_\mathrm{P}}{c_\mathrm{S}}\right)$	$\tau_{\mathrm{SI}} = 0$	$\tau_{\mathrm{SR}} = \begin{cases} 0 & , R_\mathrm{P} \le r < (c_\mathrm{P}(t - \Delta t - T) - 3R_0 + 2R_\mathrm{P}) \\ \tau_{\mathrm{SR}}(r,t) & , (c_\mathrm{P}(t - \Delta t - T) - 3R_0 + 2R_\mathrm{P}) \le r \le 3R_0 \end{cases}$

2.3. Dynamic Failure of Elastic Zones in Surrounding Rocks

(1) Zone and duration of dynamic failure

In the research area ($R_\mathrm{P} \le r \le 3R_0$) of the elastic zone, the radial dynamic stress $\sigma_{r\mathrm{d}}$ actually represents the superposed dynamic stresses brought about by P-waves (the incident and reflected) and can be expressed as:

$$\sigma_{r\mathrm{d}} = \sigma_{\mathrm{PI}} + \sigma_{\mathrm{PR}} \tag{5}$$

In the tangential direction, rock units are influenced by displacement constraints, so the dynamic tangential strain $\varepsilon_{\theta\mathrm{d}}$ equals to 0 under the effect of such stress waves. Based on Hooke's law [19], the tangential dynamic stress $\sigma_{\theta\mathrm{d}}$ (MPa) can be obtained and is given by:

$$\sigma_{\theta d} = \frac{\mu}{1-\mu} \sigma_{rd}, \tag{6}$$

where μ denotes the Poisson's ratio.

Besides, the dynamic shear stress τ_d (MPa) results from the superposition of dynamic stresses induced by S-waves (the incident and reflected) and can be written as:

$$\tau_d = \tau_{SI} + \tau_{SR}. \tag{7}$$

Based on the static stress fields in elastic zones along each direction under constant pressures [16], the strength q (MPa) of bearing structure can be expressed as:

$$q = \frac{1}{R_0+b} \left\{ \left(\frac{Q_0}{d^2} + c_{p0}\cot\phi \right) \frac{(R_0+b)^{\frac{1+\sin\phi}{1-\sin\phi}} - R_0^{\frac{1+\sin\phi}{1-\sin\phi}}}{R_0^{\frac{2\sin\phi}{1-\sin\phi}}} - c_{p0}\cot\phi \cdot b \right\} + \frac{Q_0 R_0}{d^2(R_0+b)}, \tag{8}$$

where Q_0 denotes the pre-tightening force (kN); c_{p0} means the initial cohesion (MPa) after installing the bolts, which is lower than the coal-rocks' cohesion c (MPa). The degradation of the mechanical parameters of post-peak anchorage bodies is basically reflected by their decreasing cohesion, while the change in frictional angle is small and considered as being equal to the frictional angle ϕ (°) of the coal-rock masses [20].

According to the dynamic failure principle for the dynamic and static superposition [2], the overall stresses in the research area under the effect of microseisms are given by:

$$\begin{cases} \sigma_{\theta t} = \sigma_{\theta s} + \sigma_{\theta d} \\ \sigma_{rt} = \sigma_{rs} + \sigma_{rd} \quad , \\ \tau_t = \tau_s + \tau_d \end{cases} \tag{9}$$

where σ_{rs}, $\sigma_{\theta s}$, and τ_s denote the radial, tangential, and shear stresses (MPa) under static loading, separately, while $\sigma_{\theta t}$, σ_{rt}, and τ_t represent the total tangential, radial and shear stresses (MPa), respectively.

The wave functions in every time period in Tables 1 and 2 are substituted into Equations (5)−(7), in order to attain the expressions of components of the dynamic stress in the whole time period. Then, the discrete data of stress components including σ_{rd} (r,t), $\sigma_{\theta d}$ (r,t), τ_d (r,t), σ_{rs} (r,t), and $\sigma_{\theta s}$ (r,t) were obtained in the research area ($R_p \leq r \leq 3R_0$) and time period ($0 \leq t \leq \Delta t + T + (6R_0 - 2R_p)/c_S$), based on the predefined time period dt and interval dr of space coordinate in a MATLAB program, on this basis, expressions of dynamic stress components and static stress components [16] were derived. Thereby, based on expressions of principal stresses [19] and Equation (9), the discrete data σ_1 (r,t) and σ_3 (r,t) of the principal stress components can be found by processing the discrete data of stress.

By substituting discrete data of components of principal stresses into the Mohr–Coulomb strength criterion, whether unit bodies of coal-rock masses in the studied area are destroyed or not can be judged. Figure 4 shows the corresponding flowchart. When a certain coal-rock body satisfies this failure criteria, the judgment variable J is shown as $J = 1$, or $J = 0$. Correspondingly, the dynamic failure region $R_p < r \leq R_f$ satisfying $J = 1$ in the analysis area (wherein R_f is the maximum distance between the damaged units under microseisms and the roadway center) is attained dealing with the discrete data of J. These data were obtained in accordance with the flowchart (Figure 4). Besides, the time corresponding to the moment, when the failure at $r = R_f$ happened, can be defined as the duration of dynamic failure.
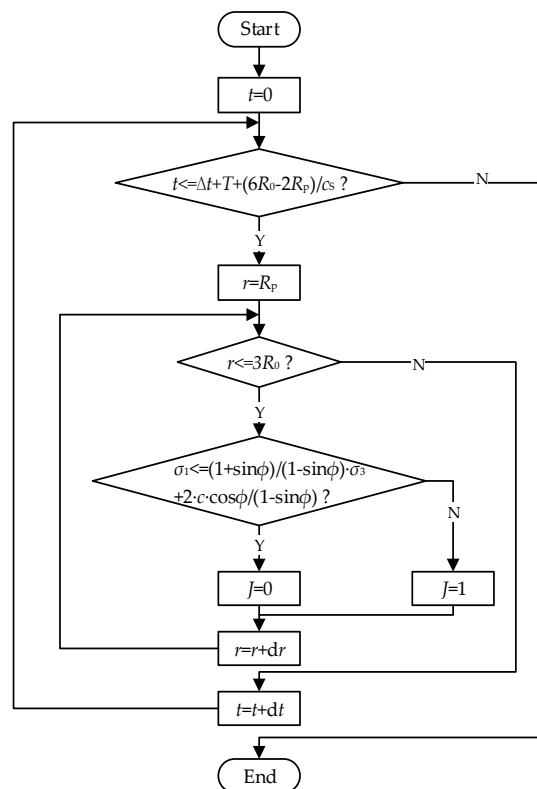
Figure 4. Flowchart for determining failures of unit bodies of coal-rock masses.

(2) Energy releasing during dynamic failures

The elastic energy density (J·m^{-3}) in surrounding rocks is expressed as:

$$e_{\mathrm{e}} = \frac{\sigma_1^2 + \sigma_2^2 + \sigma_3^2 - 2\mu(\sigma_1\sigma_2 + \sigma_1\sigma_3 + \sigma_2\sigma_3,)}{2E}, \tag{10}$$

where σ_2 indicates the intermediate principal stress (MPa) and meets $\sigma_2 = \mu(\sigma_1 + \sigma_3)$ for the plain strain problem. E refers to the elastic modulus (GPa). The discrete values of e_{e} can be acquired according to those of σ_1 and σ_3. Thus, the elastic energy in the failure region can be calculated as:

$$E_{\mathrm{e}} = \bar{e}_{\mathrm{e}} \cdot V_{\mathrm{f}}, \tag{11}$$

where $\bar{e}_{\mathrm{e}}$ and V_{f} denote the mean of e_{e} (J·m^{-3}) and the volume (m^3) of failure zones which satisfies $V_{\mathrm{f}} = S_{\mathrm{f}} \cdot 1 = \pi(R_{\mathrm{f}}^2 - R_{\mathrm{p}}^2)/2$ (for this plain strain problem, the roadway length measures 1 m along the axial direction), respectively.

The vibration energy E_{d} ($E_{\mathrm{d}} = E_{\mathrm{d}0} \cdot (L - r)^{-\eta}$ ($R_{\mathrm{p}} \le r \le R_{\mathrm{f}}$)) having influences upon failure zones can be represented as the mean $\bar{E}_{\mathrm{d}}$ (J). According to the least energy principle of impact failures [21], the corresponding energy required for impact failures is the demanded one about uniaxial failures. Therefore, the energy density required for impact failures is expressed as:

$$e_{\min} = \frac{\sigma_{\mathrm{c}}^2}{2E}, \tag{12}$$

where σ_{c} denotes the uniaxial compressive strength (MPa). The energy $E_{\min}$ (J) released in the dynamic failure can be approximately expressed as:

$$E_{\min} = e_{\min} \cdot V_{\mathrm{r}}, \tag{13}$$

According to the principle of the energy conservation, the energy E_r (J) released from a dynamic failure may be given by:

$$E_r = E_e + \overline{E}_d - E_{min}. \tag{14}$$

2.4. Resisting Impact Characteristics of Bolt-Rock Bearing Structure

It is demonstrated in previous research [21] that E_r released in failures of elastic zones is basically transformed into the kinetic energy E_k of the crushed rocks, which means $E_r = E_k$. The velocity v_f at the moment of dynamic failures is expressed as:

$$v_f = \sqrt{\frac{2E_k}{m}} = \sqrt{\frac{2E_r}{m}}, \tag{15}$$

where m denotes the mass (kg) of damaged surrounding rocks ($m = \rho V_f$).

During the time period $0 < t \leq t_d$ which the impact failure occurs, the velocity of crushed rocks grows from 0 to v_f. The impact load $f(t)$ (N) imposed on the entire damaged surrounding rocks can be obtained based on the momentum theorem and is given by:

$$mv_f - 0 = \int_0^{t_d} f(t)dt. \tag{16}$$

Owing to $f(0) = 0$ and $f(t_d) = f_m$, $f(t)$ can be equivalent on the assumption that $f(t) = Kt$ and replacing it into Equation (16), which is given by:

$$f(t) = \frac{2mv_f}{t_d{}^2}t. \tag{17}$$

Therefore, the peak impact load f_m (N) when dynamic failure takes place ($t = t_d$) in elastic zones is expressed as:

$$f_{max} = f(t_d) = \frac{2mv_f}{t_d}. \tag{18}$$

The impact load $f'(t)$ on plastic zones meets $f'(t) = f(t)$ and $f_m' = f_m$ on the basis of the interaction of forces.

It is commonly acknowledged that the kinetic energy E_k released during the failure of elastic zones travels in surrounding rocks at a fast speed and dissipates completely. Meanwhile, the impact load $f'(t)$ imposed on the plastic zone reduces rapidly from the peak f_m' and the stress state of surrounding rocks recoveries to that under static loads until E_k is dissipated completely. Under the condition, the bearing structure can be constructed only relying on the anchoring effect of bolt supporting due to that the plastic zone belongs to the post-peak region. In case of the support is damaged, the entire anchoring structure will be damaged, so the support loads of the bearing structure under the maximum shock loads are important when investigating dynamic failures of an anchored roadway.

Figure 5 shows the impact resisting analysis model for the bearing structure. In the figure, p_s, σ_{Rp} and F_n separately denote the supporting strength on boundary 3 ($r = R_0$), the uniformly distributed loads on boundary 2 ($r = R_p$), and the vertical loads on boundaries 4 and 5 under static loads. As to q_d which represents the peak stress-intensity ($r = R_p$) under dynamic loading, it meets $q_d = f_m'/\pi R_p$. In addition, p_d denotes the dynamic additional supporting strength. On boundaries 4 and 5, most of the transmitted waves that enter the limit equilibrium zone (in the post-peak state) can be dissipated during the time period for dynamic failures ($0 < t \leq t_d$), so extra dynamic loads on these boundaries are not taken into account. Furthermore, considering the fact that the limit equilibrium zone is quasi-static before it is influenced by dynamic loads ($0 < t \leq t_d$), the mechanical model can be analyzed based on the static equilibrium (inertial forces not being considered). Moreover, in the horizontal direction, the external forces can achieve the mechanical equilibrium, so this equilibrium of external forces can be realized, provided that external forces are in the equilibrium state in the vertical direction.
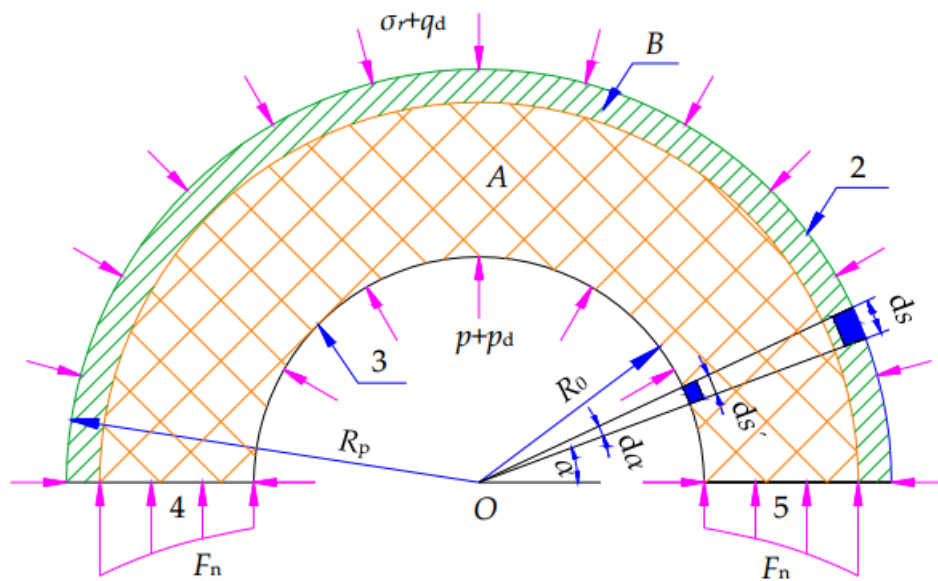
Figure 5. Impact resisting model for the anchoring structure.

In the vertical direction, the component of loads imposed on the differential arc section ds ($r = R_\text{p}$) can be obtained on condition of uniform stress $\sigma_{R\text{p}} + q_\text{d}$ at $t = t_\text{d}$ and is expressed as:

$$\text{d}F_{2y} = \left(\sigma_{R_\text{p}} + q_\text{d}\right) \sin \alpha \text{d}s, \tag{19}$$

where d$s = R_\text{p}\text{d}\alpha$, so Equation (19) can be converted into Equation (20) and rewritten as:

$$\text{d}F_{2y} = \left(\sigma_{R_\text{p}} + q_\text{d}\right) R_\text{p} \sin \alpha \text{d}\alpha. \tag{20}$$

By calculating the integral of dF_{2y} along the semicircular arc, the load component on boundary 2 can be attained in the vertical direction and is expressed as:

$$F_{2y} = \int_0^\pi \left(\sigma_{R_\text{p}} + q_\text{d}\right) R_\text{p} \sin \alpha \text{d}\alpha = 2\left(\sigma_{R_\text{p}} + q_\text{d}\right) R_\text{p}, \tag{21}$$

where α refers to the differential element for central angle to ds. Likewise, the component of loads ($r = R_0$) in the vertical direction is displayed as:

$$F_{3y} = \int_0^\pi (p_\text{s} + p_\text{d}) R_0 \sin \alpha \text{d}\alpha = 2(p_\text{s} + p_\text{d}) R_0. \tag{22}$$

In the vertical direction, the corresponding equilibrium equation of mechanical model meets:

$$F_{2y} - F_{3y} - 2F_\text{n} = 0. \tag{23}$$

By substituting Equations (21) and (22) into Equation (23), the equilibrium equation can be expressed as:

$$\left(\sigma_{R_\text{p}} R_\text{p} - p_\text{s} R_0 - F_\text{n}\right) + (q_\text{d} R_\text{p} - p_\text{d} R_0) = 0. \tag{24}$$

By substituting the equilibrium equation of static loading ($\sigma_{R\text{p}} R_\text{p} - p_\text{s} R_0 - F_\text{n} = 0$) into Equation (24), the dynamic additional supporting strength p_d (MPa) can be calculated and expressed as:

$$p_\text{d} = \frac{R_\text{p}}{R_0} q_\text{d} = \frac{R_\text{p}}{R_0} \frac{f'_\text{m}}{\pi R_\text{p}} = \frac{f'_\text{m}}{\pi R_0}. \tag{25}$$

Thereby, based on Equation (18) and $f_m' = f_m$, the expression of bolt Q_d (kN) is given by:

$$Q_d = p_d \cdot d^2 = \frac{2mv_f d^2}{\pi R_0 t_d}. \tag{26}$$

As the duration t_d of dynamic failures is considered, the time-varying characteristics can be manifested by Equation (26), which indicates that the instantaneous stress releasing is the main feature of dynamic failures.

Although the scope of failure regions and the released energies in the process of dynamic failures remain fixed under static loading (that is, when t_d is large enough), a rockburst is not likely to take place in the roadway when the energy releasing is so slow that the additional bolt resistance Q_d is small enough.

3. Case Study and Model Application

3.1. Site Description of a Coal Mine Threatened by Rockbursts

By using data recorded from in situ measurements and laboratory testing and taking the geological and mining conditions of LW402103 in the Hujiahe coal mine (location map is shown in Figure 6), Shaanxi, China, as the research object, the track roadway of LW402103 buried 400 m underground was studied. Figure 7 and Table 3 separately show the geologic column section of LW402103 and the mechanical parameters of coal and rock layers. By using the fully-mechanized top-coal caving multi-slicing mining method, the top slice (13 m thick) was firstly mined, followed by arrangements of the roadways along the floor of top slice, and the bottom coal of 10 m thick was left to serve as the bottom slice. As a semicircular section (Figure 8), the track roadway was 5 m wide (radius R_0 of the roadway in the above analysis model was 2.5 m), presenting a roadway height of 4 m. In addition, by using the bolt and mesh supports, the anchor length and bolt length a are 0.5 m and 2.4 m, respectively. Moreover, the yield strength, diameter, and breaking strength (250.8 kN as the ultimate resistance [Q]) of bolt supports were 500 MPa, 22 mm, and 660 MPa, separately. Also, 60 kN of prestressing force Q_0 was applied on the bolts and the bolts were arranged with the row and line spacings d both being 0.7 m.

Figure 6. Location of the Hujiahe coal mine (Xianyang, Shaanxi, China).
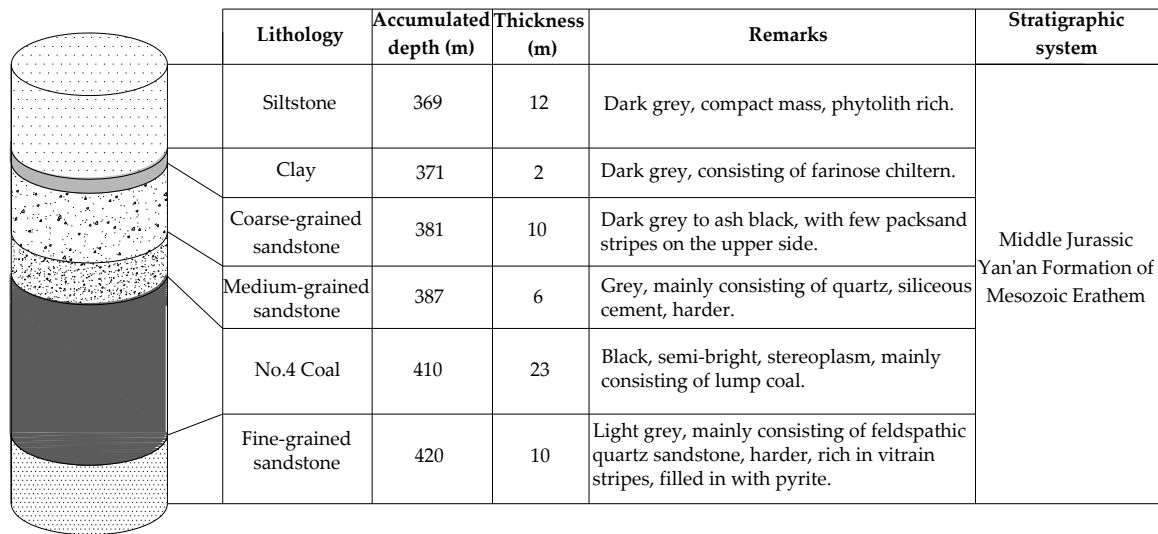
Figure 7. Geologic column of LW402103, showing the geological information (lithology, thickness, depth, age, etc.) for roofs, coal seam and floor.

Table 3. Mechanical parameters of coal and rock layers.

Lithology	Thickness (m)	Density, ρ (kg/m^3)	Elastic Modulus, E (GPa)	Uniaxial Compressive Strength, σ_c (MPa)	Poisson's Ratio, μ	Cohesion, c (MPa)	Frictional Angle, ϕ (°)
Siltstone	12	2348	13	29	0.25	3.9	34
Clay	2	2125	6	21	0.28	2.4	31
Coarse-grained sandstone	10	2535	14	32	0.23	4.2	36
Medium-grained sandstone	6	2363	8	26	0.24	2.9	32
No. 4 coal	23	1350	2	10	0.35	1.2	30
Fine-grained sandstone	10	2458	16	35	0.20	5.6	38
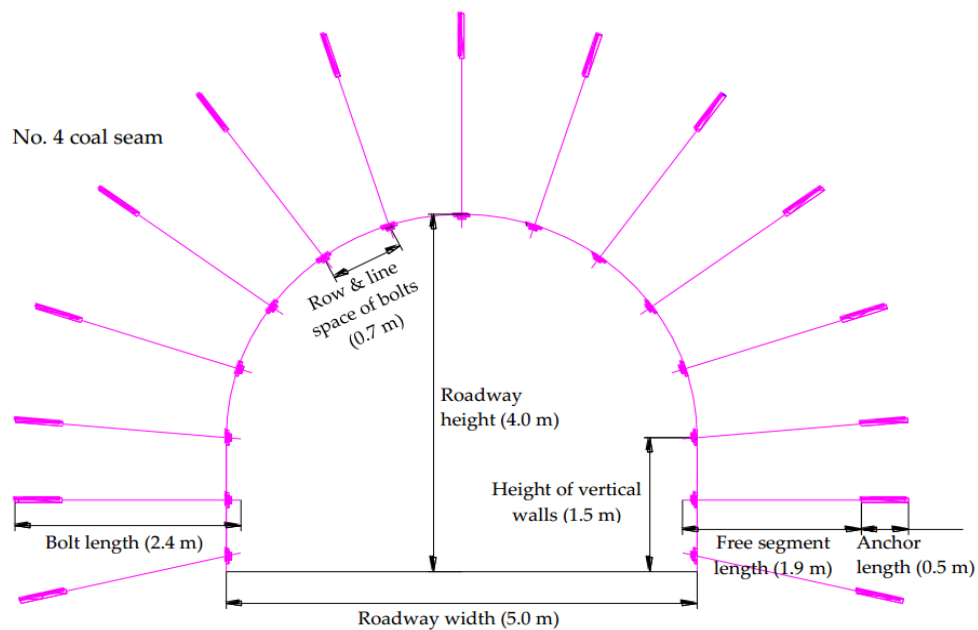
Figure 8. Track roadway's supporting parameters, including bolt length, anchor length and row and line space of bolts.

Two rockbursts took place during the excavation of the track roadway (Figure 9 and Table 4). Figure 10 displays one of the in situ failure modes for rockbursts (occurring at 19:34 p.m. on 18 April 2014). The rockburst (affected range of 17 m) was triggered by a microseismic event of 4.85×10^5 J. Due to the dynamic failure strengths of anchoring structure exceeding the surface protection ability of wire nets, the anchoring body was influenced and the crushed rocks were ejected to the roadway. In Figure 10, the seriously damaged bolts are marked with red circles. After discussing the in situ failure situation, it is inferred that the impact failures of bolt supporting led to the deformation and even whole burst of the anchoring structures.
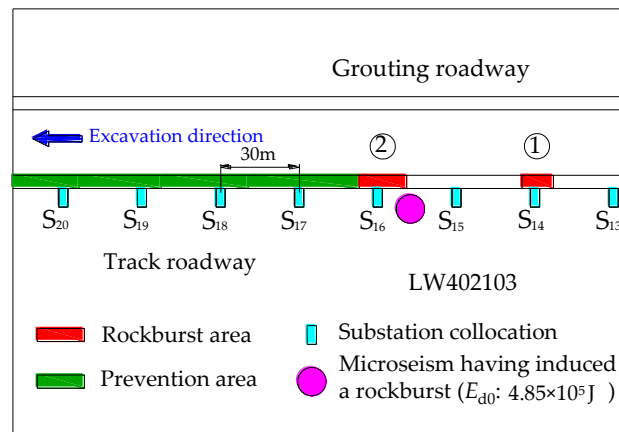
Figure 9. Rockburst and prevention of the track roadway in LW402103.
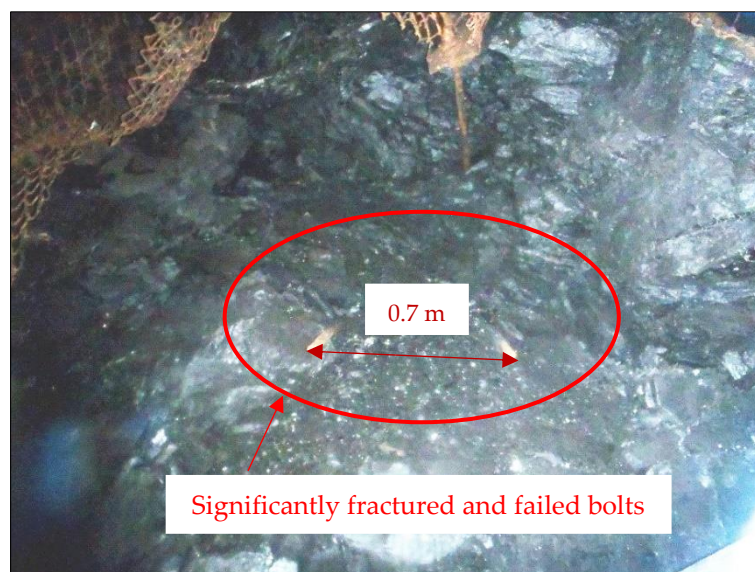
Figure 10. In situ failures of a rockburst (occurring at 19:34 p.m. on 18 April 2014).

There was a monitoring and forecasting system adopted on site to ensure the mining safety of LW402103, combining with the Microseismic Monitoring System (named ARAMIS from Poland) and the On-line Measurement System of Bolt Resistances (Version No. YHY60). Therefore, the bolt resistances and microseismicity were all monitored in a real-time manner, to supply useful measurement results for analyzing the engineering case. Therefore, three-dimensional coordinates and energies of microseismic events can be acquired in real-time by the ARAMIS System. The substations, arranged on bolt tails in the sidewalls, were used for measuring bolt resistances. In addition,

these substations, containing the stress sensor, data recorder, etc. (Figure 11), were installed at the equal spacing of 30 m, as shown in Figure 9.

Table 4. Rockburst occurrence of track roadway in LW402103.

Number of Rockbursts	Date and Time	Microseismic Energy (J)	Influence Range (m)	Remarks
1	7:11 a.m. on 31 March 2014	1.82×10^4	12	Three bolts in the roof were loose with convergence ranging from 0.32 m to 0.41 m.
2	19:34 p.m. on 18 April 2014	4.85×10^5	17	Four bolts in the sidewall were fractured and surrounding rocks were ejected to the roadway.
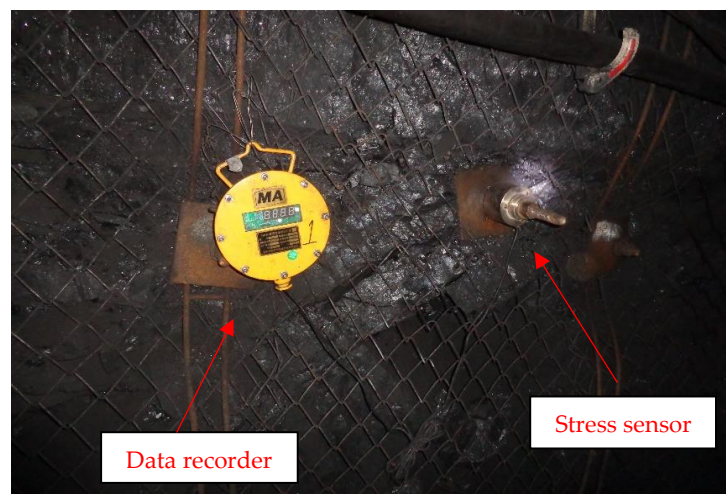
Figure 11. In situ installation of on-line substations for monitoring bolt resistances.

By taking the rockburst occurring at 19:34 p.m. on 18 April 2014 in the track roadway as an example, it was found that the microseismic event (with a dominant frequency of 15 Hz) triggering this rockburst released energies of 4.85×10^5 J based on the results from ARAMIS microseism monitoring system. Besides, this event taking place in the roof (12 m siltstone) was approximately 30 m (12 R_0) from the center of roadway. The average values of propagation speeds c_p and c_s of P- and S-waves in a coal-rock mass are 4000 m/s and 2300 m/s, respectively. Based on existing research results [18], the medium attenuation coefficient η in rocks can be equal to 1.526.

3.2. Rockburst Criterion and Factors Analysis

According to monitoring results of the microseismicity and relevant parameters of the track roadway, various results are acquired. The predefined dt and dr were set as 2.5×10^{-4} s and 2.5×10^{-2} m in the MATLAB program. Table 5 shows the relevant results (R_p, b, q, ($R_p - R_f$), t_d and Q_d) of the study case (a rockburst occurring in track roadway of LW402103).

Table 5. Calculation results of a roadway rockburst based on the dynamic failure analysis model (a case occurring at 19:34 p.m. on 18 April 2014 in the track roadway of LW402103).

Radius of Plastic Zone, R_p (m)	Thickness of Bearing Structure, b (m)	Strength of Bearing Structure, q (MPa)	Dynamic Failure Range ($R_p - R_f$) in Elastic Zones (m)	Duration of Dynamic Failures, t_d (s)	Additional Impact Resistance, Q_d (kN)
4.58	1.72	3.03	4.58 − 5.05	2.075×10^{-2}	46.43

Despite of the utilization of bolt supports after excavating the roadway, the surrounding rocks lost equilibrium. Besides, the deformation of the rocks surrounding the roadway induced by dilatancy would be further enhanced with bolt resistances that increased correspondingly until the anchorage achieved a new equilibrium state. According to the results of the interior precast initial damaged rock samples loading-unloading test and triaxial compression test, the strength degradation model of damaged surrounding rocks in the deep roadway, represented by the plastic parameter ε^{ps}, was established, which can be directly applied to the theoretical analysis and numerical simulation [22]. Moreover, during the dilatant deformation, the strength of surrounding rocks constantly decreases to the residual strength, which is mainly shown as a reduction in their cohesion [19]. Correspondingly, the attenuation model of post-peak cohesion can be given by:

$$\frac{c_p}{c} = 0.458 + 0.499 \times e^{-\varepsilon^{ps}/0.000452}, \tag{27}$$

where c_p and ε^{ps} indicate the post-peak cohesion (MPa) and the plastic strain parameter, respectively. Based on this attenuation model, the post-peak cohesion c_p constantly attenuates to the residual cohesion c_{pr} with increasing plastic strain. Based on experimental results of interior precast initial damaged rock samples loading-unloading tests [22], when $\varepsilon^{ps} = 0.007$, $c_p = c_{pr} = 0.458c$.

The anchoring surrounding rocks under conditions of static loading showed slow dilatancy deformations and attenuations of rock strength. Additionally, due to reinforcement of bolt supports, stabilization can generally be realized before the cohesion degrades to the residual cohesion, that is, the stable cohesion c_s under static load meets $c_s > c_{pr}$. However, it was demonstrated in previous research [18] that dynamic loads are able to accelerate the surrounding rock damages, and thus not only the cohesion is rapidly decreased, but also the stable cohesion c_s' in a stable state after dynamic disturbance is closer to the residual cohesion c_{pr}, (namely $c_s > c_s' \geq c_{pr}$). Moreover, it should be noted that post-peak cohesion under the stable state after dynamic disturbance commonly results from release of stress from the surrounding rocks under conditions of static load and dynamic disturbance.

To elaborate the cohesion degradation of anchorage bodies under dynamic loads, the damage factor D of cohesion is defined as:

$$D = 1 - \frac{c_p}{c_{p0}}, \tag{28}$$

where c_{p0} represents the initial cohesion (MPa) when bolts are installed and meets $c_{pr} \leq c_p \leq c_{p0}$. For the post-peak anchorage body, its initial cohesion c_{p0} can be about 0.7 times of cohesion c [22]. Owing to the surrounding rocks being affected by multiple microseisms, the degradation of cohesion is caused by the cumulative effects of dynamic loads and $D \propto \sum\limits_{i=1}^{n} E_{d0}$ (where n is the number of microseisms).

As active supports, surrounding rocks are reinforced actively by applying the bolt pre-tightening force. It can be considered that during the service life of such bolt supports, the strength q (Equation (8)) of the anchoring bearing structure is generally unchanged. The strength degradation and dilatancy of surrounding rocks in steady states after being subjected to impact disturbances are, in fact, brought about by the joint effects of the stress releasing from surrounding rocks under static loads and the accumulative effects of multiple dynamic disturbances. Therefore, the relevant bolt resistance is defined as the static cumulative resistance Q_s. In addition, Q_s constantly increases so as to adapt to the dilatancy-induced deformation and decreasing cohesion caused by the stress release of surrounding rocks under conditions of static loads and the dynamic disturbance.

According to the essential parameters of the LW402103 track roadway, D is in the range of $0 \leq D \leq 0.35$ according to $c_{pr} \leq c_p \leq c_{p0}$. By substituting $q = 3.03 \times 10^6$ MPa (Table 5) into Equation (8), the relationship between Q_s and c_p is given by:

$$Q_s = \frac{\cot\phi(b - K)d^2}{K + R_0}c_p + \frac{q(R_0 + b)d^2}{K + R_0}, \tag{29}$$

where $K = \dfrac{(R_0+b)^{\frac{1+\sin\phi}{1-\sin\phi}} - R_0^{\frac{1+\sin\phi}{1-\sin\phi}}}{R_0^{\frac{2\sin\phi}{1-\sin\phi}}}$ ..

By combining Equations (28) and (29), the relationship between Q_s and D was obtained and is shown in Figure 12. The static cumulative resistance linearly increases with the degradation of surrounding rock strength, which satisfies $Q_s = 462 \cdot D + 60$. It should be noted that the rock properties are actually not degraded gradually, but rather go (due to loads and bursts) to "point of breakdown", which happens most often along the fault zone(s). While this curve (Figure 12) is mainly based on Equation (29), only presenting the theoretical relationship between Q_s and D. Therefore, the real degradation of surrounding rock strength is not shown in Figure 12. Under dynamic loads, even though the damages to surrounding rocks are aggravated, so that the surrounding rock strength reaches the residual strength (corresponding to the residual cohesion c_{pr}), the peak static cumulative resistance Q_{sm} is 217 kN, which is still smaller than the ultimate resistance $[Q]$ (250.8 kN). Therefore, static cumulative resistance Q_s resulted from the strength degradation and the deformation of surrounding rocks caused by the stress release under static loads and dynamic disturbances is unlikely to result in impact failures of bolt supporting. The greatest disparity between static and dynamic failures of bolt supports lies in that the Q_d is generated in the impact failure process of elastic zones. Therefore, under dynamic loads, the overall real-time bolt resistance Q equals to the sum of static accumulative resistance Q_s and additional impact resistance Q_d, namely, $Q = Q_s + Q_d$.
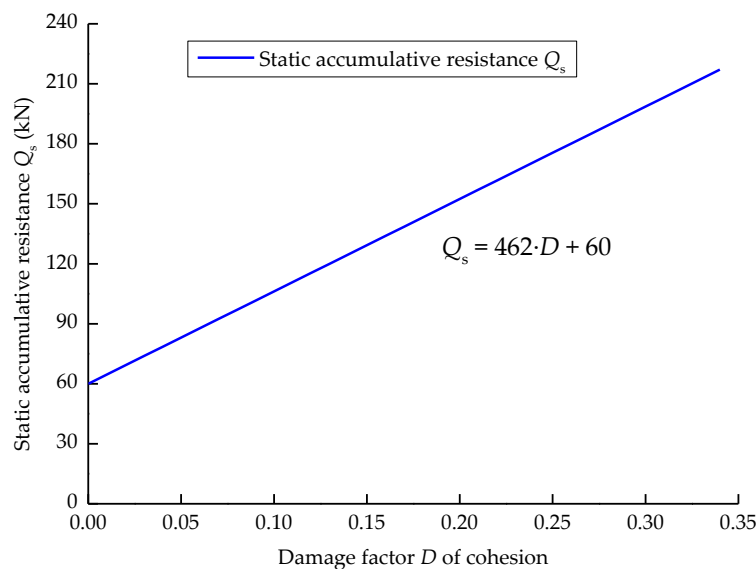

Figure 12. Relationship between static accumulative resistance Q_s and damage factor D of cohesion.

In order to study the variation of bolt resistance caused by unstable additional impact resistance Q_d, the variation of Q_d with microseismic energy release E_{d0} (10^4 J $\leq E_{d0} \leq 10^6$ J) were obtained (Figure 13), according to the relevant parameters of track roadway. It can be seen from Figure 13 that Q_d grows from 8.32 to 69.06 kN with E_{d0}, with its proportion in Q increasing from 3.33% to 27.60%, which satisfies the functional relation $Q_d = -3 \times 10^{-11} \cdot E_{d0}^2 + 9 \times 10^{-5} \cdot E_{d0} + 8.39$. Even if Q_d induced by the microseismic events releasing energy surpassing 10^6 J merely takes a small percentage in Q in which Q_s is the major component. Obviously, Q_s sets the foundation for, while Q_d is the practical inducement for, impact failures occurring to bolt supporting. Besides, both of them are necessary for predicting rockburst in a roadway. Accordingly, the following shows the criterion for judging a rockburst in an anchored roadway support structure:

$$Q > [Q] (Q = Q_s + Q_d). \tag{30}$$

In other word, dynamic failures of bolt supporting are likely to occur if the overall real-time bolt resistance is greater than the ultimate bolt resistance. This will be followed by the destruction of the complete anchor structure, which accords with the in situ observed situations of rockbursts, as shown in Figure 10.

The overall real-time resistance Q was monitored by using the on-line substations about bolt resistances. Supposing that the overall real-time resistances were Q_1 and Q_2, separately before, and after, the microseismic event, the in situ measured Q_d' induced by dynamic loads can be calculated as $Q_d' = Q_2 - Q_1$. In addition, the theoretical Q_d can be obtained according to Equations (11)−(18) and (26), based on monitoring data of microseismic events. Furthermore, the distribution of microseismic energies as well as the theoretical Q_d and in situ measured Q_d' in a time period can be attained by calculating and processing the monitoring data about bolt resistances and microseisms.

$$Q_d = -3\times10^{-11} \cdot E_{d0}{}^2 + 9\times10^{-5} \cdot E_{d0} + 8.39$$
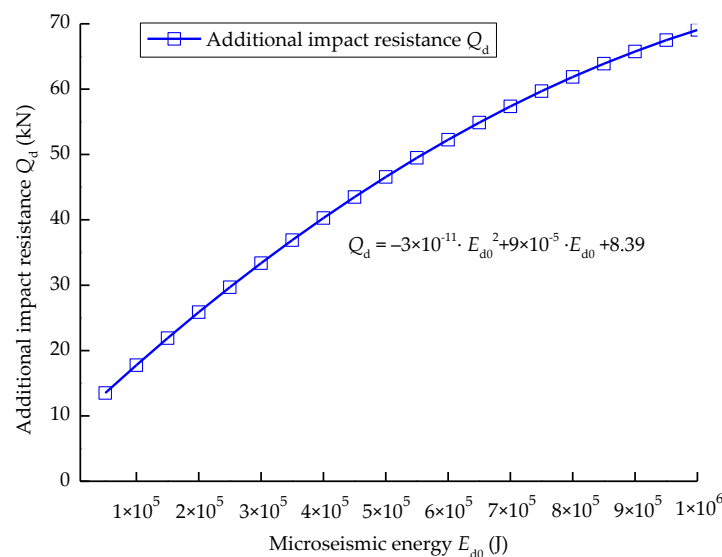
Figure 13. Relationship between microseismic energy E_{d0} and additional impact resistance Q_d.

During the period of time before the rockburst, sub-station S_{16}, as shown in Figure 9, near the microseismic sources was applied to collect distributions of microseismic energies (>10^4 J) and additional impact resistances in the vicinity of the heading face of the track roadway from 12 to 18 April 2014 (Figure 14). The result reveals that the in situ measured Q_d' were basically close to theoretical values (Q_d). Moreover, the greater the microseismic energy was, the higher the in situ measured Q_d'. The result coincided with the theoretical relationship between E_{d0} and Q_d (Figure 13).

Figure 15 illustrates the time history curve of overall bolt resistance Q during five minutes before the microseism monitored by the sub-station S_{16}. This microseism happening at 19:34 p.m. on 18 April 2014 and releasing 4.85×10^5 J of energies had induced a rockburst. It was speculated that Q had experienced multiple, small fluctuations under the action of some events with low energies (<10^4 J) before the occurrence of the rockburst while it remained at 210.5 kN around (i.e., Q_s). When the event of large energy (4.85×10^5 J) happened, Q_d' was computed to be 40.3 kN in accordance with in situ measurement, approaching Q_d (46.43 kN) attained from the theoretical calculation. Considering bolt supports had been destroyed when Q equaled to [Q], 40.3 kN was just the lowest practical value of Q_d'. The anchoring structure was destroyed completely in case that the overall real-time bolt resistance Q rose to (or even exceeded) the ultimate bolt resistance [Q] (250.8 kN). The results demonstrate that the in situ measurement results accorded with the corresponding rockburst criterion presented from Equation (30).
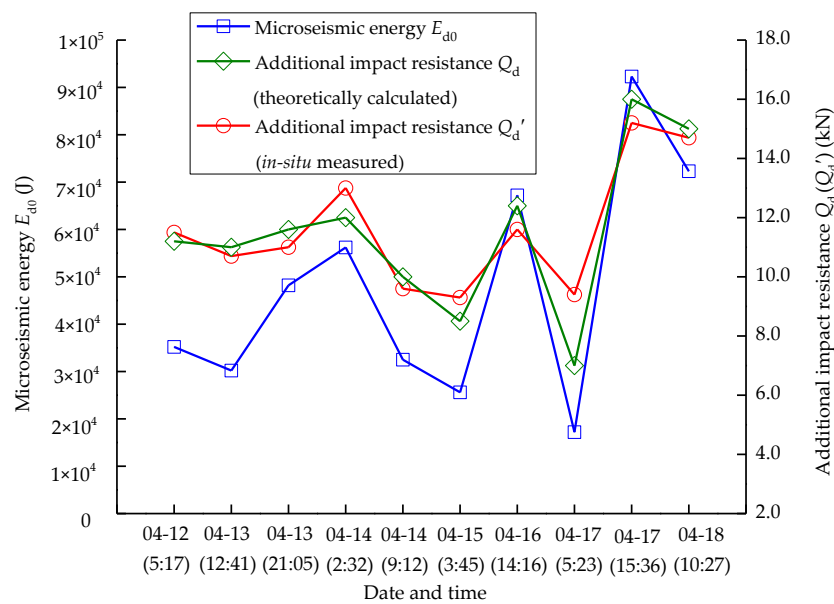
Figure 14. Distributions of microseismic energies ($>10^4$ J) and additional impact resistances close to the heading face of track roadway (12−18 April 2014).

To study the impacts of parameters of roadway support (including the roadway radius R_0 along with the row and line space d of bolts) upon loading of bolt supports (the static cumulative resistance Q_s, additional impact resistance Q_d and strength q of bolted-rock bearing structures) were analyzed (Figure 16). As shown in Figure 16a, functional relations between roadway radius R_0 and loading (q, Q_s and Q_d) of bolt supports are given by:

$$\begin{cases} q = 0.34 \cdot R_0{}^2 - 2.53 \cdot R_0 + 7.21 \\ Q_s = -6.64 \cdot R_0{}^2 + 80.22 \cdot R_0 - 27.11 \\ Q_d = 17.16 \cdot R_0 + 3.52 \end{cases} \quad , \tag{31}$$

As shown in Figure 16b, functional relations between row and line space d of bolts and loading (q, Q_s and Q_d) of bolt supports are given by:

$$\begin{cases} q = 2.61 \cdot d^2 - 6.91 \cdot d + 6.60 \\ Q_s = 84 \cdot d^2 + 80.85 \cdot d + 39.38 \\ Q_d = 213.49 \cdot d^2 - 150.89 \cdot d + 47.17 \end{cases} \quad , \tag{32}$$

As the R_0 and d increase, q reduces gradually, while Q_s and Q_d increase. When d grows from 0.5 m to 1.0 m, Q_d and Q_s increase by 84.67 kN and 102.72 kN, respectively, while q decreases by 1.55 MPa. Moreover, when R_0 grows from 1.8 m to 3.0 m, Q_d and Q_s increase by 20.59 kN and 57.20 kN, while q decreases by 1.12 MPa. The smaller the radius of roadway and bolt spacings are, the greater the strength of the bearing structures while the lower the static cumulative resistance and additional impact resistance, which can enhance the supporting effect to a certain degree. Additionally, the bolt spacings exhibit more significant influences on the loading of the bolted supports than that of the roadway radius.
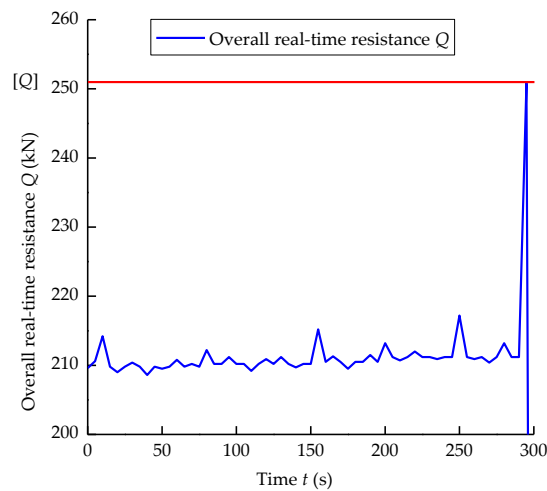
**Figure 15.** Time-history curve of overall real-time resistance Q (measured by substation S_{16}).

$Q_s = -6.64 \cdot R_0^2 + 80.22 \cdot R_0 - 27.11$

$q = 0.34 \cdot R_0^2 - 2.53 \cdot R_0 + 7.21$

$Q_d = 17.16 \cdot R_0 + 3.52$

(**a**)

$Q_s = 84 \cdot d^2 + 80.85 \cdot d + 39.38$

$q = 2.61 \cdot d^2 - 6.91 \cdot d + 6.60$

$Q_d = 213.49 \cdot d^2 - 150.89 \cdot d + 47.17$
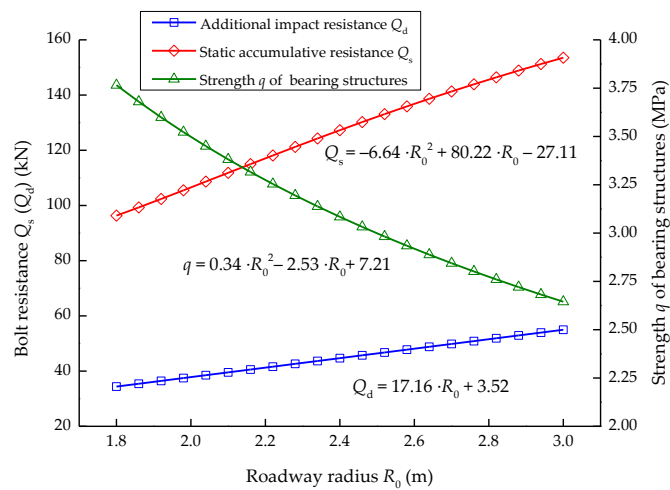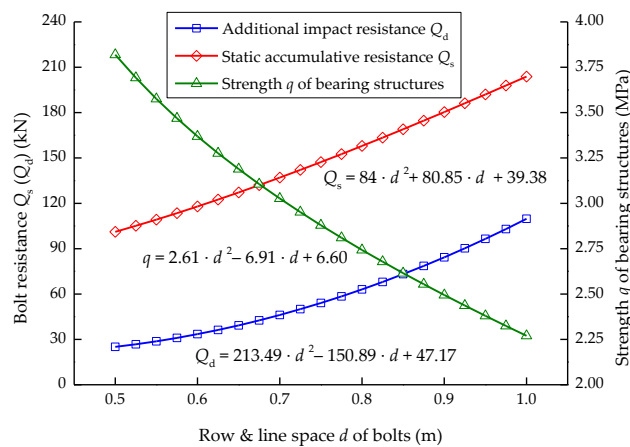
(**b**)

Figure 16. Influences of parameters of roadway supports on loading of bolt supports: (**a**) Roadway radius R_0; (**b**) Row and line space d of bolts.

3.3. Preventing Measures and Tests

Based on the aforementioned analysis, preventing measures are suggested from following aspects:

(1) Applying pressure-relief methods. According to the research results in Figure 13, the larger the vibration energy, the greater the additional impact resistance Q_d and the more seriously the anchored surrounding rocks are damaged and deformed, which can lead to a higher static cumulative resistance Q_s. Considering this, the vibration energy E_d, which anchored surrounding rocks bear, needs to be decreased: E_d is mutually decided by the attenuation coefficient η (namely $E_d = E_{d0} \cdot (L - r)^{-\eta}$) and microseismic energy E_{d0}. Pressure-relief measures can decline the vibration energy E_d which the anchoring structure bears, by decreasing the microseismic energy E_{d0} and augmenting the attenuation coefficient η. To be specific, the vibration energy can be decreased by applying deep hole presplitting blasting in hard roofs and enlarging the attenuation coefficient by drilling large-diameter destress boreholes.

(2) Optimizing parameters of roadway supporting. To improve the impact resistance of anchoring structures, the roadway radius and bolt spacings can be decreased. Whereas, the radius of roadway is commonly not easily changed and it has insignificant effects on the impact resistance. For this reason, reducing bolt spacings, which is the more feasible measure, is expected to be used. Additionally, as a crucial factor determining the occurrence of rockbursts (based on Equation (30)), the ultimate bolt resistance [Q] can be observably increased by utilizing bolts with the larger diameter and higher strength.

Considering the construction difficulty degree of preventative measures and the necessary cooperation with the tunneling process, the simplest and effective methods for the track roadway were using the large-diameter destress boreholes and decreasing the bolt spacing. After the rockburst on 18 April 2014, the large-diameter destress boreholes were carried out on the track roadway of LW402103. The locations where destress boreholes were drilled in the coal seam included the heading face and sidewalls of the roadway in the top slice (Figure 17), and the bottom slice (Figure 18), of No. 4 coal seam. Tables 6 and 7 provide the design parameters of these pressure-relief measures. Besides, the support density of track roadway also grew by decreasing the row and line space of bolts from 0.7 m to 0.6 m.
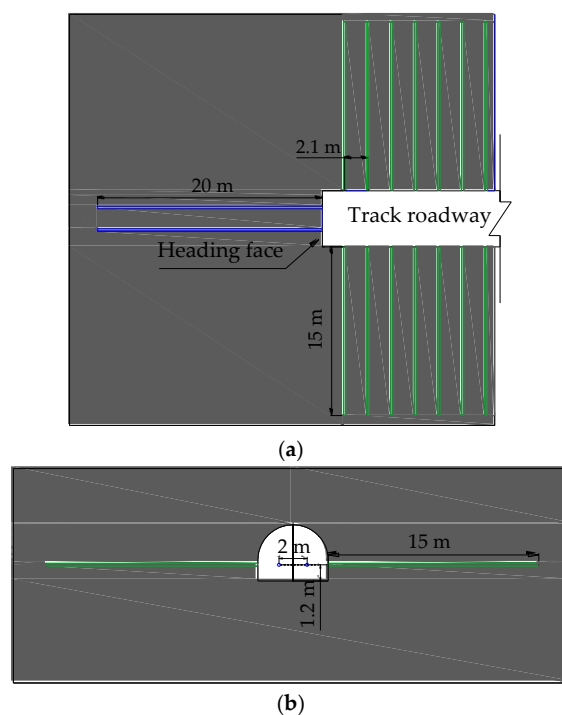

Figure 17. Large-diameter destress boreholes at the heading face and roadway sidewalls in the top slice of coal seam: (**a**) Planar graph; (**b**) Profile along the roadway tendency.

(**a**)

(**b**)
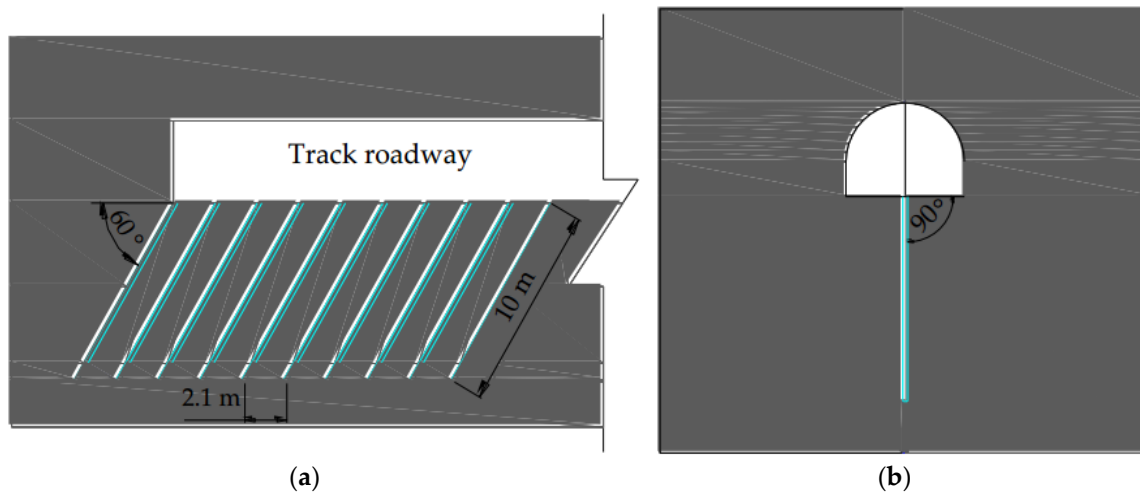
Figure 18. Large-diameter destress boreholes at the heading face and roadway sidewalls in the bottom slice of coal seam: (**a**) Profile along the roadway strike; (**b**) Profile along the roadway tendency.

Table 6. Design parameters for large-diameter destress boreholes in the top slice of coal seam, constructed at the heading face and roadway sidewalls.

Construction Position	Angle of Depression (°)	Borehole Length (m)	Borehole Diameter (mm)	Borehole Spacing (m)
Heading face	0	20	113	2
Roadway sidewalls	0	15	113	2.1

Table 7. Design parameters for large-diameter destress boreholes in the bottom slice of coal seam.

Angle of Depression (°)	Borehole Length (m)	Borehole Diameter (mm)	Borehole Spacing (m)
60	10	113	2.1

After a period of time of taking preventing measures, substation S_{18} near the microseismic sources was used to obtain distributions of microseismic energies and additional impact resistances close to the heading face of track roadway from 3 to 7 May 2014. Therein, the theoretical Q_d were obtained based on the modified bolt spacing (0.6 m) and above-mentioned calculation methods. Accordingly, the distribution curves (3−7 May 2014) of the microseismic energies (>10^4 J) and additional impact resistances in the prevention area were shown in Figure 19. It can be seen from Figure 19 that the changing regulation of in situ measured Q_d' was broadly similar to those of theoretical values Q_d (only considering the improved row and line space of bolts (0.6 m)). While the former was comparatively less than the latter, whose average resistance accounted for about 77% of theoretical results. These indicate that reducing the row and line space of bolts can decline the additional impact resistance effectively. Besides, the drilling of large-diameter destress boreholes can raise the attenuation coefficient η and further decrease the vibration energy E_d which anchoring bodies bear. Accordingly, the in situ prevention effect can be better with the combination of taking pressure-relief measures and optimizing parameters of roadway support.
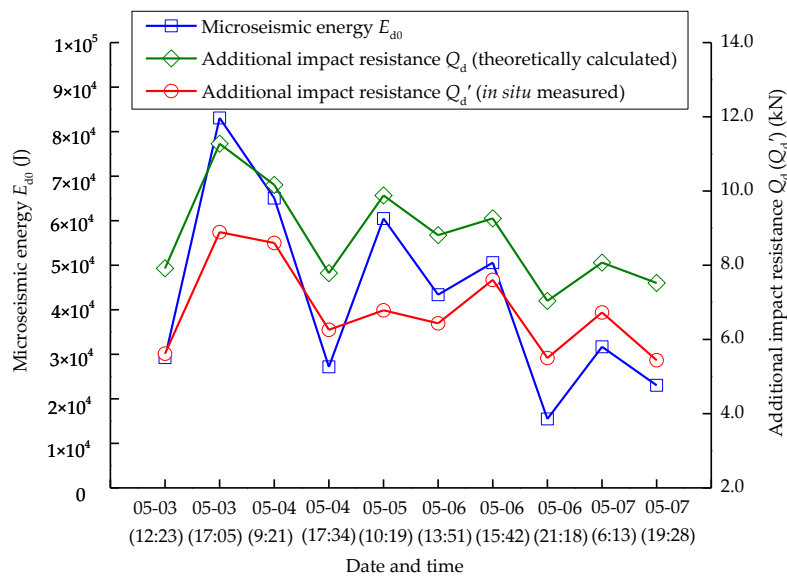
Figure 19. Distributions of microseismic energies ($>10^4$ J) and additional impact resistances in the prevention area (3−7 May 2014).

4. Conclusions

This study established a mechanical model for the bearing structure of roadways under mining-induced dynamic loads. Based the case of LW402103 of the Hujiahe coal mine, the results of theoretical analysis were verified and the application of preventive measures has been deemed effective for coal mines.

As a representative dynamic disaster encountered during coal mining, the rockburst seriously impacts the safety and production of coal mines. Most (approximate 85%) rockbursts, induced by microseisms, occur in anchoring roadways. However, the interaction between dynamic loads and roadway surrounding rocks has not been comprehensively considered in existing studies. Therefore, the dynamic failure analysis for the mechanism of roadway rockbursts is necessary.

The research object of mechanical model is the roadway in coal seams (namely No. 4 coal seam in the case study). The dimensional and seismic strength scales of this study are limited to mine field scale and microseisms in coal mines.

The in situ application was implemented by taking preventing methods for the track roadway in LW402103 of the Hujiahe coal mine, which contained taking pressure-relief methods and optimizing parameters of roadway supporting. Pressure-relief methods were carried out by applying deep hole presplitting blasting in hard roofs and drilling large-diameter destress boreholes in coal seams. Additionally, the support density of track roadway also grew by decreasing the row and line space of bolts from 0.7 m to 0.6 m. The in situ measured data after taking preventing measures indicated that the average resistance of in situ measured Q_d' accounted for about 77% of the theoretical Q_d, showing an effective application of preventive measures.

References

1. Petr, K.; Petr, W. Stress changes and seismicity monitoring of hard coal longwall mining in high rockburst risk areas. *Tunn. Undergr. Space Technol.* **2018**, *81*, 237–251. [CrossRef]
2. He, J.; Dou, L.M.; Gong, S.Y. Rock burst assessment and prediction by dynamic and static stress analysis based on micro-seismic monitoring. *Int. J. Rock Mech. Min. Sci.* **2017**, *93*, 46–53. [CrossRef]
3. Hatzor, Y.H.; He, B.G.; Feng, X.T. Scaling rockburst hazard using the DDA and GSI methods. *Tunn. Undergr. Space Technol.* **2017**, *70*, 343–362. [CrossRef]
4. Lawson, H.E.; Tesarik, D.; Larson, M.K.; Abraham, H. Effects of overburden characteristics on dynamic failure in underground coal mining. *Int. J. Min. Sci. Technol.* **2017**, *27*, 121–129. [CrossRef]
5. Zuo, J.P.; Chen, Y.; Cui, F. Investi gation on mechanical properties and rock burst tendency of different coal-rock combined bodies. *J. China Univ. Min. Technol.* **2018**, *47*, 81–87. [CrossRef]
6. Wang, G.F.; Dou, L.M.; Cai, W. Unstable energy triggering mechanism of rock burst. *J. China Univ. Min. Technol.* **2018**, *47*, 190–196. [CrossRef]
7. Feng, J.J.; Wang, E.Y.; Chen, X. Energy dissipation rate: An indicator of coal deformation and failure under static and dynamic compressive loads. *Int. J. Min. Sci. Technol.* **2018**, *28*, 397–406. [CrossRef]
8. Mark, C. Coal bursts that occur during development: A rock mechanics enigma. *Int. J. Min. Sci. Technol.* **2018**, *28*, 35–42. [CrossRef]
9. Horyl, P.; Snuparek, R. Reinforcing measures of steel roadway support in rockburst prone areas. *Arch. Min. Sci.* **2012**, *57*, 193–208. [CrossRef]
10. Coşkun, I.; Engin, H.; Ozmutlu, A. Dynamic stress and displacement in an elastic half-space with a cylindrical cavity. *Shock Vib.* **2011**, *18*, 827–838. [CrossRef]
11. Davis, C.A.; Lee, V.W.; Bardet, J.P. Transverse response of underground cavities and pipes to incident SV waves. *Earthq. Eng. Struct. Dyn.* **2001**, *30*, 383–410. [CrossRef]
12. Gao, M.S.; Zhao, Y.C.; Wen, Y.Y.; Cheng, Z.C.; Quan, X.C. Stress and energy criterion of the roadway destruction subjected to disturbance type rock burst and its practice. *J. China Coal Soc.* **2016**, *41*, 808–814. [CrossRef]
13. Aleksandrova, N.I.; Ayzenberg-Stepanenko, M.V.; Sher, E.N. Modeling the elastic wave propagation in a block medium under the impulse loading. *J. Min. Sci.* **2009**, *45*, 427–437. [CrossRef]
14. Pan, Y.S.; Xiao, Y.H.; Li, Z.H. Study of tunnel support theory of rockburst in coal mine and its application. *J. China Coal Soc.* **2014**, *39*, 222–228. [CrossRef]
15. He, M.C.; Jia, X.N.; Colic, M. Experimental study of rockbursts in underground quarrying of Carrara marble. *Int. J. Rock Mech. Min. Sci.* **2012**, *52*, 1–8. [CrossRef]
16. Zhang, Y.D. Study on Bearing Characteristic of Composite Bolt-Rock Bearing Structure and Its Application in Roadway Bolting Design. Ph.D. Thesis, China University of Mining and Technology, Xuzhou, China, 2013.
17. Brady, B.H.G.; Brown, E.T. Energy, Mine stability, mine seismicity and rockbursts. In *Rock Mechanics for Underground Mining*, 3rd ed.; Kluwer Academic Publishers: Dordrecht, The Netherlands, 2004; pp. 277–285.
18. He, J.; Dou, L.M.; Cai, W. In situ test study of characteristics of coal mining dynamic load. *Shock Vib.* **2015**, 1–8. [CrossRef]
19. Boresi, A.P.; Chong, K.P. *Elasticity in Engineering Mechanics*, 3rd ed.; Wiley & Sons: New York, NY, USA, 2011; pp. 65–68.
20. He, M.C.; Leal, E.; Sousa, R.; Müller, A. Analysis of excessive deformations in tunnels for safety evaluation. *Tunn. Undergr. Space Technol.* **2015**, *45*, 190–202. [CrossRef]
21. Zhao, Y.S.; Feng, Z.C.; Yang, D. Three-dimensional fractal distribution of the number of rock-mass fracture surfaces and its simulation technology. *Comput. Geotech.* **2015**, *65*, 136–146. [CrossRef]
22. Niu, S.J.; Jing, H.W.; Hu, K. Numerical investigation on the sensitivity of jointed rock mass strength to various factors. *Int. J. Min. Sci. Technol.* **2010**, *20*, 530–534. [CrossRef]